PHYSICAL REVIEW D VOLUME 25, NUMBER 1 1 JANUARY 1982

Properties of the low-mass ωp enhancement observed in $p_{\uparrow}p \to p\omega p$ at 11.75 GeV/c

M. W. Arenton, D. S. Ayres, R. Diebold, E. N. May,
L. Nodulman, J. R. Sauer,* and A. B. Wicklund
Argonne National Laboratory, Argonne, Illinois 60439
(Received 18 August 1981)

Samples of the reaction $p_{\uparrow}p \to p\omega p$, consisting of 20000 and 1000 events at 11.75 and 6 GeV/c, respectively, were obtained using the Zero Gradient Synchrotron polarized proton beam and the Effective Mass Spectrometer. A narrow enhancement near threshold is seen in the ωp mass distribution. The t distribution of this enhancement shows a pronounced dip near $t = -0.2$ GeV^2 at both beam momenta, suggesting that ω exchange is the dominant production mechanism. The joint-decay-angular-distribution moments and polarization correlations have been determined as functions of ωp mass. Amplitude analysis of these moments indicates that the low-mass enhancement is due to the high-mass tails of spin-parity $\frac{3}{2}^-$ and $\frac{3}{2}^+$ states below ωp threshold. Polarization correlations consistent with zero provide evidence for the lack of resonant behavior in the low-mass enhancement itself.

I. INTRODUCTION

We report results based on samples of 20000 and 1000 events of the reaction

$$p_{\uparrow}p \to p\omega p \ , \tag{1}$$

which were obtained using the Zero Gradient Synchrotron (ZGS) polarized proton beam at 11.75 and 6 GeV/c and the Effective Mass Spectrometer. Earlier experiments[1-12] examining the ω-N system using a variety of incident beam particles have had much lower statistical precision: the best such experiment, done with π^+ and π^- beams, had 5000 events.[1] Several of these experiments observed a relatively narrow enhancement near threshold in the ωp mass distribution. Attempts to determine the spin and parity content of the enhancement have been at best qualitative.[13] The observation of this enhancement is confirmed in the present experiment and a detailed examination of its production and decay properties is presented, based on analysis of the angular-distribution moments of the ωp and $\omega \to \pi^+\pi^-\pi^0$ decay systems. Analysis of these moments leads to a determination of the spin and parity content of the enhancement.

Study of channels such as ωp provides new information on the subject of baryon-resonance spectroscopy. Most of our current knowledge of the spectrum of nonstrange baryon resonances is based on analysis of π-nucleon scattering, especially on phase-shift analysis of π-N elastic scattering. One long-standing problem in this field has been the apparent absence of some of the states predicted by simple quark models. The model of Isgur and Karl[14,15] has recently been quite successful in explaining this problem by showing that only those states that have been observed should couple to πN while the remaining states should be decoupled from the πN system. This model also does reasonably well in predicting the mass splittings of the various states.

In order to detect the states that do not couple to the πN system, one must rely on production experiments, using the various possible t-channel exchanges as "beams". In particular, in the present experiment, we shall present evidence that suggests the ωp system is produced by ω exchange and that thus, in a sense, what is being studied is ωp elastic scattering.

The experimental method is presented in Sec. II. In Sec. III the mass and t distributions and the angular-distribution moments are presented. Section IV discusses the production mechanism and the determination of the spin and parity content of the low-mass enhancement.

II. EXPERIMENTAL METHOD

A. Apparatus and trigger

The experiment used the polarized proton beam from the ZGS incident on a 25-cm-long liquid hydrogen target. The polarization was either transverse to the beam direction or longitudinal; longitudinal polarization was obtained by rotating the spin of the transversely polarized beam from the ZGS[16] with superconducting solenoids and the final bending magnets in the beam transport. About half of the data were taken with transverse and half with longitudinal polarization. The sign of the polarization (up or down, parallel or antiparallel) was reversed on alternate ZGS pulses. The absolute magnitude of the polarization was about 60%. For the transverse running the beam polarization was measured in the experimental apparatus by recording a sample of pp elastic-scattering events. For the longitudinal running the beam polarization was monitored using a carbon polarimeter located in the external proton beam just after its extraction from the ZGS and a liquid hydrogen polarimeter operated by the polarized target group.

Events of the reaction $pp \rightarrow p\pi^+\pi^-\pi^0 p$ were measured by the Effective Mass Spectrometer (EMS), shown in Fig. 1. The trajectories of the incident beam particles were measured by four sets of multiwire proportional chambers. The large-aperture magnetic spectrometer[17] used five sets of magnetostrictive-readout wire spark chambers ($K1-K5$) to measure the momenta of the forward produced p, π^+, and π^-. The direction of the recoil proton was measured by the recoil-proton detector[18] which consisted of two cylindrical multiwire proportional chambers coaxial with the target. Anode wires parallel to the beam direction measured the azimuthal direction of the recoil trajectories, and cathode-strip readouts provided longitudinal coordinates along the anode-wire direction. The π^0 was not detected.

The trigger for this experiment was primarily intended to select events of the final state $p\pi^+\pi^-p$ and imposed the following requirements. A good beam particle was defined by a beam telescope and hole counters to veto halo. An interaction in the target was signaled by the absence of the beam particle in a 2.5-cm-square beam-veto counter just downstream of the spectrometer magnet and either a count in the HOLE counter just downstream of the target or $\geq$ two-particle pulse height in the dE/dx counter which covered the hole in the HOLE counter. Exactly three hits were required in the 40-counter scintillator hodoscope downstream of the magnet. At most one hit, corresponding to the recoil proton, was allowed in the box of veto counters surrounding the target on four sides and in the eight magnet veto counters lining the aperture of the spectrometer magnet. The large CO_2-filled Čerenkov counter[19] at the

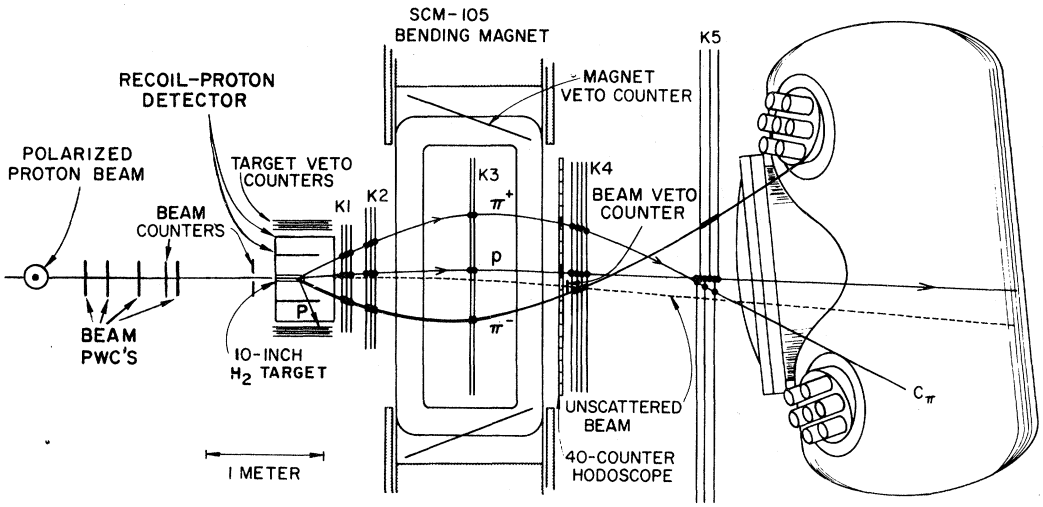

FIG. 1. Plan view of the Argonne Effective Mass Spectrometer. $K1$ through $K5$ are sets of magnetostrictive-readout wire spark chambers. C_π is a CO_2-filled threshold Čerenkov counter with π threshold 3.0 GeV/c. In the region around the liquid hydrogen target the transverse dimensions have been exaggerated for clarity.

downstream end of the apparatus was not used in the trigger but was used in the offline analysis to distinguish between the π^+ and proton.

Data were read in by a CAMAC system and recorded on magnetic tape by a PDP 11/34 computer. About 10% of the events were sent on-line to an EMR 6050 computer that used a simplified version of the off-line track-reconstruction and analysis program to reconstruct the event kinematics. About 50 triggers were recorded per 800-msec spill of about 60 000 beam particles. In addition to the principal trigger, a random sample of beam triggers, elastic-scattering triggers, and special triggers designed to monitor trigger biases were recorded. A total of 2.1×10^7 triggers were recorded in the course of the experiment.

B. Selection of $p\omega p$ events

After the momentum vectors of the forward tracks were reconstructed from the spark-chamber information, the following procedure was used to isolate the sample of events of $pp\to p\omega p$. In order to reconstruct the direction of the recoil proton reliably, azimuthal (anode-wire) hits were required in both the inner and outer cylinders of the recoil-proton detector. Recoil track directions were then calculated from the production-vertex location, determined from the measurement of the beam and forward-going tracks, and from the recoil detector using the two azimuthal measurements and one or two longitudinal measurements.

For events with the desired topology of two positive and one negative forward tracks and at least one recoil track, we first removed events of the reaction $pp\to p\pi^+\pi^-p$ by means of cuts on the three available kinematic constraints. Events were rejected if the square of the missing mass calculated from the beam and forward p, π^+, and π^- was within 0.5 GeV^2 of the square of the proton mass, and if the measured azimuthal angle and the cotangent of the polar angle of the recoil differed from the values predicted by the $p\pi^+\pi^-p$ kinematics by less than 0.1 and 0.08, respectively. These tests were made for both possible assignments of the positive tracks to the proton and the π^+.

We next searched for events consistent with the $p\pi^+\pi^-\pi^0p$ hypothesis. First the large downstream Čerenkov counter was used to identify one of the positive particles as the proton. If either of the positive tracks was the only track above pion threshold in one of the four cells of the counter and that cell fired, then that track was identified as the π^+. Otherwise the track with the higher momentum was taken to be the proton. Examination of kinematically constrained $p\pi^+\pi^-p$ events showed that this procedure gave the wrong assignment for about 5% of the events; this effect was included in the Monte Carlo used to determine the acceptance.

Calculations were then made to determine the π^0 momentum vector and the magnitude of the recoil-proton momentum using the zero-constraint (0C) kinematics of the reaction $pp\to p\pi^+\pi^-\pi^0p$. Only events with at least one physical solution to the quadratic ambiguity were retained. Also for events where more than one possible recoil track had been found in the recoil detector, where an extra track might be due to a δ ray or to noise in the chambers, the 0C calculation was tried for all possible recoil tracks and all acceptable solutions retained. However, events with three or more possible recoil tracks were discarded.

The quadratic ambiguities were partially resolved by imposing the following criteria on each solution. For each solution the recoil momentum was required to be sufficient for the track to escape from the hydrogen target and pass through the two cylinders of the recoil detector. The veto counter array which surrounded the target on four sides consisted of alternating layers of lucite, lead, and scintillator to stop soft δ rays, convert photons, and detect charged particles. Events were rejected if any veto counters fired which were inconsistent with the observed recoil-track direction. For each event, track solutions were retained provided the recoil momentum and range were consistent with the veto-counter hits; thus, if a counter fired, the momentum had to exceed a minimum range cut, and if a counter did not fire, the momentum had to be below a maximum range cut. These requirements successfully resolved the kinematic ambiguity in about half of the events; both solutions were retained in the subsequent analysis for the remaining events.

A cut was made on the $\pi^+\pi^-\pi^0$ Dalitz-plot distribution to further improve the purity of the sample of ω events. The Dalitz-plot distribution for the decay of a 1^- state such as the ω is strongly peaked at the center of the plot and falls to zero at the edges.[20] We found that the background under the ω signal was peaked near the edges of the plot. A cut was made selecting events within a circle of radius 0.2 unit from the center of the plot (where in the nonrelativistic approximation the boundary

of the plot is a circle of radius 0.33 unit).

Figure 2 shows the $\pi^+\pi^-\pi^0$ mass distribution after all these selections have been applied, for those events with four-momentum transfer $-t$ from the beam to the $\pi^+\pi^-\pi^0 p$ system between 0.075 and 1.0 GeV^2. A prominent ω peak is evident. A fit to this distribution using a Gaussian for the ω and a cubic polynomial for the background yields a mass of 0.784 GeV and a width $\sigma=0.034$ GeV. The ratio of signal to background for the whole range of ωp masses is better than one to one at small $|t|$, but the background is worse for higher $|t|$. As a function of ωp mass for all t the signal to background is better than one to one at small ωp mass, but is worse for higher ωp mass.

In order to improve the resolution on the ωp mass and on four-momentum transfer t, events were fitted to constrain the mass of the $\pi^+\pi^-\pi^0$ system to the central mass of the ω. Kinematic quantities such as the ωp mass, t, and the decay angles describing the breakup of the ω and the ωp systems were derived from the fitted four vectors; the raw $\pi^+\pi^-\pi^0$ mass obtained from the unfitted momenta was retained for each event, in order to determine the background under the ω peak. For example, to obtain the ωp mass spectrum shown in Fig. 3, the events were binned in the fitted ωp mass and for each ωp mass bin the raw $\pi^+\pi^-\pi^0$ mass

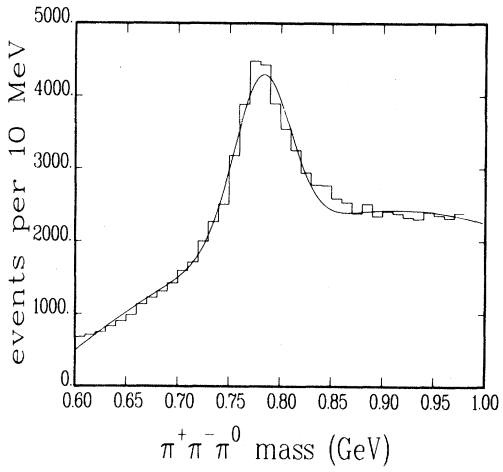

FIG. 2. The $\pi^+\pi^-\pi^0$ mass for the reaction $pp \to p\pi^+\pi^-\pi^0 p$ at 11.75 GeV/c for all events with $-t$ between 0.075 and 1.0 GeV^2. Both solutions of the quadratic ambiguity are included if the ambiguity could not be resolved by the methods described in the text. The curve is a fit to a Gaussian and cubic-polynomial background.

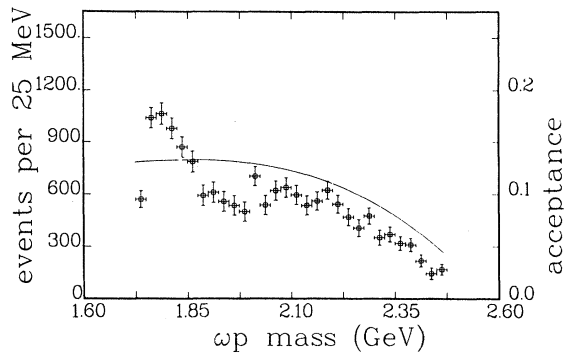

FIG. 3. The distribution of the number of events of the reaction $pp \to p\omega p$ vs ωp mass for the $-t$ range 0.075 to 1.0 GeV^2. No acceptance corrections have been applied to the data points. The solid curve shows the acceptance for isotropic decays.

spectrum was fit to a Gaussian plus cubic polynomial background to determine the number of ω's present. In this fit the central value and width of the Gaussian were held fixed at the values obtained from the fit to the overall sample of data. This was justified by analytic calculations based on the known properties of the spectrometer, which showed negligible variation of the $\pi^+\pi^-\pi^0$ mass resolution with ωp mass and t.

C. Acceptance corrections and determination of moments

To determine the cross section and angular-distribution moments of the data, the acceptance of the spectrometer had to be unfolded. The method used a maximum-likelihood technique similar to that described in detail in a previous publication,[21] with the following differences. The moments calculated in the present experiment are functions of two sets of angles, namely the angles describing the breakup "N^*" $\to \omega p$, and the decay $\omega \to \pi^+\pi^-\pi^0$. Also in this experiment the integrals of products of the angular functions times the acceptance were calculated by Monte Carlo techniques rather than by analytic methods.

The Monte Carlo program generated events of $pp \to p\omega p$ with subsequent decay of the $\omega \to \pi^+\pi^-\pi^0$. Events were generated flat in the four decay angles. A flat distribution in ωp mass was generated and the t distribution was taken to agree approximately with the t distribution observed in the raw data. The $\omega \to \pi^+\pi^-\pi^0$ decay was gen-

erated according to the ω Breit-Wigner mass distribution and with the proper 1^- particle Dalitz-plot distribution. The particles were tracked through the spectrometer and hits in the appropriate scintillation counters generated. The Monte Carlo tracks were not subjected to multiple scattering or resolution smearing. However, the aperture cuts imposed on the Monte Carlo tracks and also on the tracks of the actual events were set to be more stringent than the physical apertures of the spectrometer. (About 15% of the actual event sample was excluded by these cuts.) Events passing the aperture cuts were subjected to the same event-selection program as the real data.

The acceptance for events generated isotropically has the following general characteristics. It is flat as a function of ωp mass out to about 2.2 GeV, above which it drops off as is shown by the solid curve in Fig. 3. At low t the acceptance is restricted by the requirement that the recoil proton escape from the target and penetrate the recoil detector. From $|t|$ of 0.1 to about 1.0 GeV^2, the acceptance is reasonably flat. To describe the breakup of the ωp system and the subsequent decay of the ω, we used a t-channel coordinate frame as defined in the Appendix. In this frame the acceptance is slowly varying as a function of the $\omega\to\pi^+\pi^-\pi^0$ decay angles. It is also nearly flat in the azimuthal angle describing the orientation of the ω momentum vector, but is strongly forward peaked in the polar angle between the ω direction and the z axis, although it is nonzero for all values of the angle. The average isotropic acceptance for the ωp mass range 1.725 to 2.475 GeV and $|t|$ range 0.075 to 1.0 GeV^2 is about 16%.

The acceptance-corrected event rates were converted to cross-section values using the beam flux obtained from scaling the beam telescope. Corrections to this flux for beam proportional chamber inefficiency, extra beam tracks within the event and accidental veto-counter firing were applied. The flux at 11.75 GeV/c gave a sensitivity for 100% acceptance of 6.9 events per nb.

Several other nongeometric corrections were also applied in order to extract cross sections. The efficiency of the recoil-proton detector was measured using recoil protons from kinematically constrained $pp\to p\pi^+\pi^-p$ and pp elastic scattering events and found to be $93\pm5\%$. Conversions of photons from π^0 decay in the 0.024 radiation lengths of material in the spectrometer leads to a correction of 4%. Correction for interactions of the forward p, π^+, and π^- in the hydrogen target and scintillators and spark chambers is 9%. Inefficiency of the spark chambers and of the reconstruction programs requires a correction of $(9\pm6)\%$.

Background subtractions were made to obtain the final sets of moments. Statistics did not permit a detailed fit of the $\pi^+\pi^-\pi^0$ mass spectrum for each moment in each bin. Instead, the region 0.733 to 0.833 GeV in the $\pi^+\pi^-\pi^0$ mass distributions was used to define the "peak", and the moments of the "wing" events in the mass ranges 0.683 to 0.733 and 0.833 to 0.883 were subtracted.

The cross section for production of a ωp system with subsequent decay of the ω to $\pi^+\pi^-\pi^0$ by a polarized proton beam incident on an unpolarized target may be written as

$$\frac{d^6\sigma}{dm\,dt\,d\Omega\,d\Omega'}=\frac{1}{16\pi^2}\sum_{L,l,n}\{a^L_{ln}[f_n((2L+1)(2l+1))^{1/2}\cos n\varphi'\,d^l_{n0}(\theta')d^L_{0n}(\theta)]$$
$$+P_{||}c^L_{ln}[(2(2L+1)(2l+1))^{1/2}\sin n\varphi'\,d^l_{n0}(\theta')d^L_{0n}(\theta)]$$
$$+P_\perp b^L_{ln}[(2(2L+1)(2l+1))^{1/2}\cos(\psi+\varphi+n\varphi')d^l_{|n|0}(\theta')d^L_{1n}(\theta)]\}\,, \qquad (2)$$

where $f_0=1$, $f_1=f_2=\sqrt{2}$, $P_{||}$ ($P_\perp$) is the parallel (transverse) beam polarization, and the sum extends over $L=0,\ldots,L_{\max}$, $l=0$ or 2, and $n=0,1,2$ for the unpolarized and $P_{||}$ terms, and $n=0,\pm1,\pm2$ for the $P_\perp$ terms. With our normalization, a^0_{00} gives the cross section integrated over Ω and Ω'. The derivation of Eq. (2) and the definitions of the angles ψ, θ, θ', φ, and φ' are given in the Appendix. Briefly, θ and φ describe the orientation of the ω momentum vector in the ωp rest frame; θ' and φ' describe the decay normal for the $\omega\to\pi^+\pi^-\pi^0$ decay; ψ gives the orientation of the transverse polarization vector relative to the production normal ($\psi=0$ denotes polarization along the normal, $\psi=\pi/2$ denotes polarization in the scattering plane). We have assumed t-channel heli-

city conservation in order to limit the observables to a tractable number, and we have verified that the unpolarized cross sections are flat in φ, consistent with Eq. (2).

The sets of moments a_{ln}^{L}, b_{ln}^{L}, c_{ln}^{L} were determined from the data for various mass and t bins by the acceptance-correction procedure described earlier. Terms up through $L=4$ were kept. The acceptance-corrected moments may be compared to the θ, φ, θ', and φ' projections of the data by weighting the sample of accepted Monte Carlo events by Eq. (2). An example of this comparison is shown in Fig. 4. Including moments up through $L=4$ gives a χ^2 of 1.37 per degree of freedom when the data are analyzed in 10 ωp mass bins and a t bin from -0.075 GeV^2 to -0.2 GeV^2.

III. FEATURES OF THE DATA

Figure 3 shows the background-corrected distribution of the data in ωp mass for $|t|$ from 0.075 to 1.0 GeV^2, before correction for acceptance. A considerable enhancement at low mass is evident. Figure 5 shows the momentum transfer distribution, corrected for acceptance, for all events with ωp mass between 1.725 and 2.475 GeV. The t dependence shows a break and change in slope at $|t|=0.2$ GeV^2; fits to the form e^{Bt} give $B=16.3\pm1.0$ GeV^{-2} for $|t|<0.2$ GeV^2, and $B=1.4\pm0.2$ GeV^{-2} for $|t|>0.2$ GeV^2. Figure 6 shows the same distribution, but only for events in the enhancement in the ωp mass distribution ($m_{\omega p}<1.9$ GeV). The distribution is again very steep at small $|t|$ and much less so at larger $|t|$ (exponential slopes of 21.5 ± 1.9 GeV^{-2} and 2.3 ± 0.4 GeV^{-2} below and above $|t|=0.2$ GeV^2), and suggests the presence of a dip around $|t|=0.2$ GeV^2.

We measure the forward-hemisphere cross section to be 27 ± 6 μb for the reaction $pp\to p\omega p$ at 11.75 GeV/c in the ωp mass range 1.725 to 2.475 GeV and $|t|$ range 0.075 to 1.0 GeV^2, for $\omega\to\pi^+\pi^-\pi^0$. Extrapolating to the full mass and t range yields the total cross section. Extrapolations using the measured t slopes were made for $|t|$ larger than 1.0 GeV^2 and for $|t|$'s below the acceptance cutoff at 0.075 GeV^2. Correction was

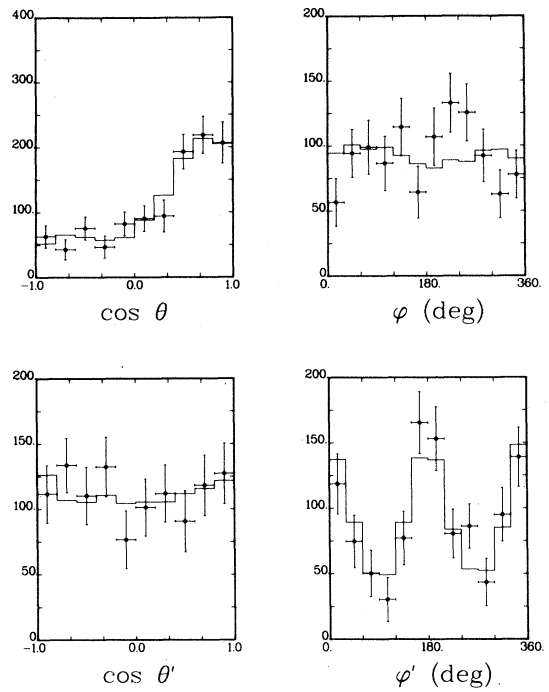

FIG. 4. The raw event distributions in the decay angles θ, φ of the ωp system in the t-channel frame and the decay angles θ', φ' of the $\omega\to\pi^+\pi^-\pi^0$ system in the s-channel frame for the ωp mass bin 1.775 to 1.825 GeV. The solid histogram shows the distribution of the sample of accepted Monte Carlo events weighted by the moments obtained for this bin.

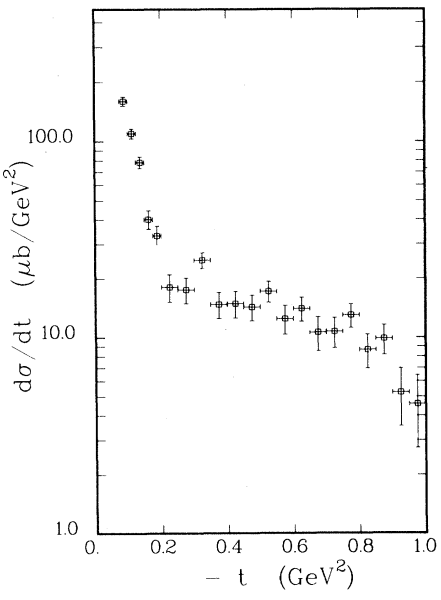

FIG. 5. The acceptance-corrected differential cross section $d\sigma/dt$ for the reaction $pp\to p\omega p$ with subsequent ω decay to $\pi^+\pi^-\pi^0$ at 11.75 GeV/c with ωp mass between 1.725 and 2.475 GeV. The errors shown are statistical.

made for ωp masses greater than the acceptance cutoff assuming the distribution to remain flat out to the kinematic limit. After multiplying by a factor of 2 to account for both forward and backward hemispheres and correcting for the branching fraction of ω decay to $\pi^+\pi^-\pi^0$, we obtain a total cross section of 160 ± 35 μb. The error is dominated by experimental systematics and uncertainties in the extrapolations. Our value of the total cross section is in good agreement with the value of 150 ± 10 μb measured at 12 GeV/c by Blobel *et al.*[22]

Figure 7 shows the acceptance-corrected angular distribution moments defined above as functions of ωp mass for the $|t|$ range from 0.075 to 0.2 GeV^2. The bin sizes have been chosen so as to have about 1000 events above background in each bin. In the a_{00}^0 moment (which is the acceptance-corrected cross section) the low-mass enhancement is somewhat less obvious than in the raw data due to the larger acceptance corrections for the higher-mass region. The a_{00}^1 moment is seen to start out positive at threshold and cross over to negative values at higher mass. The a_{00}^2 moment shows positive values in the low-mass region, dropping to zero at higher mass. The a_{20}^2, a_{21}^2, and a_{22}^2 moments show small values at threshold, increasing to a peak near 2.1 GeV. The a_{00}^3 moment is consistent with zero near threshold, becoming nonzero above 1.9 GeV; this moment is interesting because it requires the presence of orbital D waves in the ωp system. The a_{20}^3, a_{21}^3, and a_{22}^3 moments are all nonzero in the region of the enhancement, dropping to zero at higher mass. All of the transverse and longitudinal polarization correlations are consistent with zero. The interpretation of these behaviors will be discussed later.

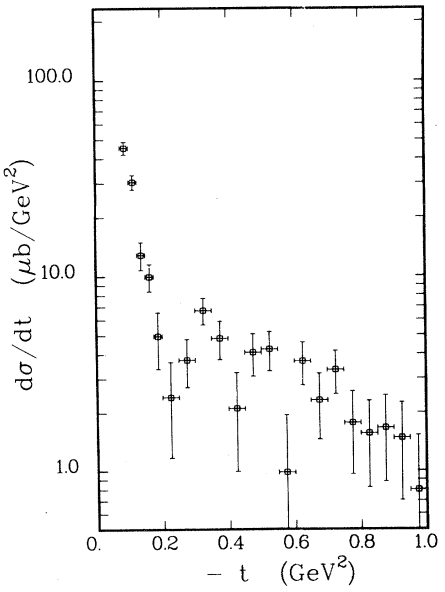

FIG. 6. The acceptance-corrected differential cross section $d\sigma/dt$ for the reaction $pp\to p\omega p$ with subsequent ω decay to $\pi^+\pi^-\pi^0$ at 11.75 GeV/c with ωp mass between 1.725 and 1.9 GeV.

IV. PHYSICS ANALYSIS

A. Production mechanism

The break or dip structure in the t distribution around 0.2 GeV^2 is similar to that observed in nucleon diffraction dissociation $NN\to NN\pi$, with the $N\pi$ mass close to threshold.[23,24] This behavior was interpreted by Berger and Pirila as evidence for absorptive corrections to the π-exchange Deck mechanism.[25] In our reaction, a π-exchange Deck amplitude could be present, but other mechanisms for exciting the low-mass ωp system include Pomeron and ω exchange. The properties of the ω-exchange amplitude have been studied in elastic $K^\pm p$ and pp and $\bar{p}p$ scattering[26]; there the elastic cross section differences demonstrate the existence of a zero in the imaginary part of the ω-exchange contribution at $t=-0.2$ GeV^2. Thus a strong ω-exchange amplitude would qualitatively explain the t distribution in our reaction.

We have examined the energy dependence of $pp\to p\omega p$ to test for consistency with ω exchange. The total cross sections versus beam momentum are shown in Fig. 8, based on data from earlier experiments.[11,12,22,27–34] We do not include our point in this figure because of the many assumptions and extrapolations needed to extract the total cross section; the cross sections in the plot include all ωp masses and not just the low-mass region, except for the two highest energy points which correspond to central values of center-of-mass rapidity.[34] The data in the region above 10 GeV/c are fit by the form $p_{\rm lab}{}^{-n}$ with $n=0.77\pm0.07$. If the two highest energy points are excluded the best fit gives $n=0.86\pm0.18$. A value of $n=1$ is expected from ω exchange. Diffractive production would yield a much smaller n, for instance diffractive production of the A_1 meson proceeds with $n=0.42\pm0.04$.[35]

A small sample of data was taken at 6 GeV/c in the present experiment. The apparatus and trigger

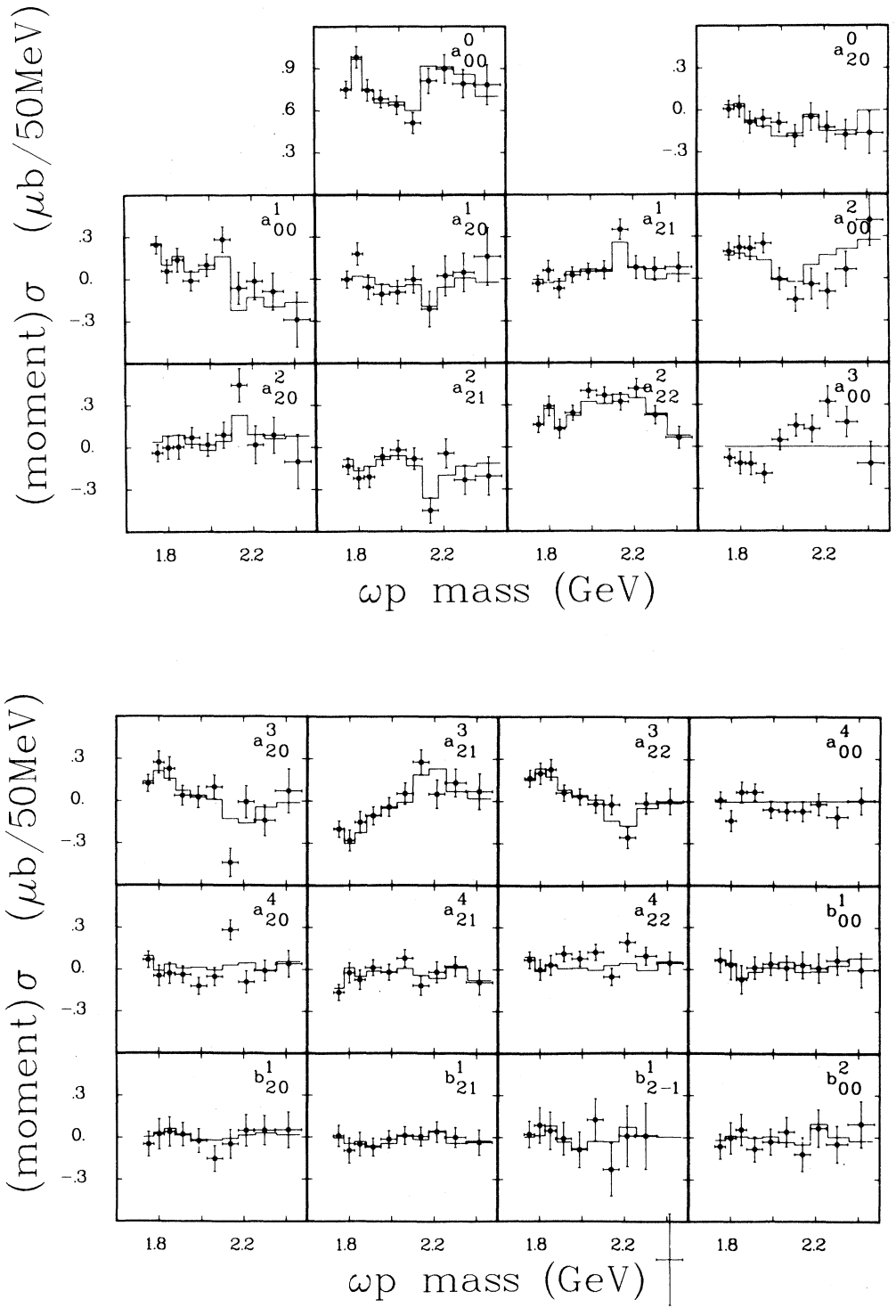

FIG. 7. The angular-distribution moments a_{ln}^{L} and polarization correlations b_{ln}^{L} and c_{ln}^{L} defined in the text as functions of ωp mass for the $-t$ range 0.075 to 0.2 GeV^2. The histograms show the fit to the data of solution A of the amplitude analysis.

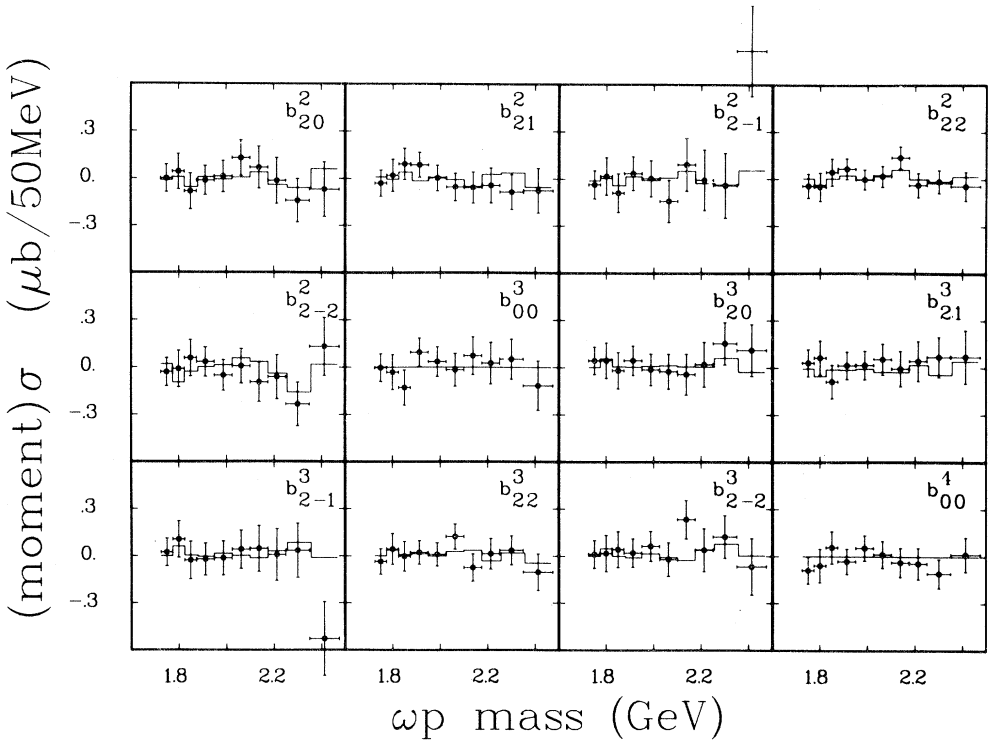

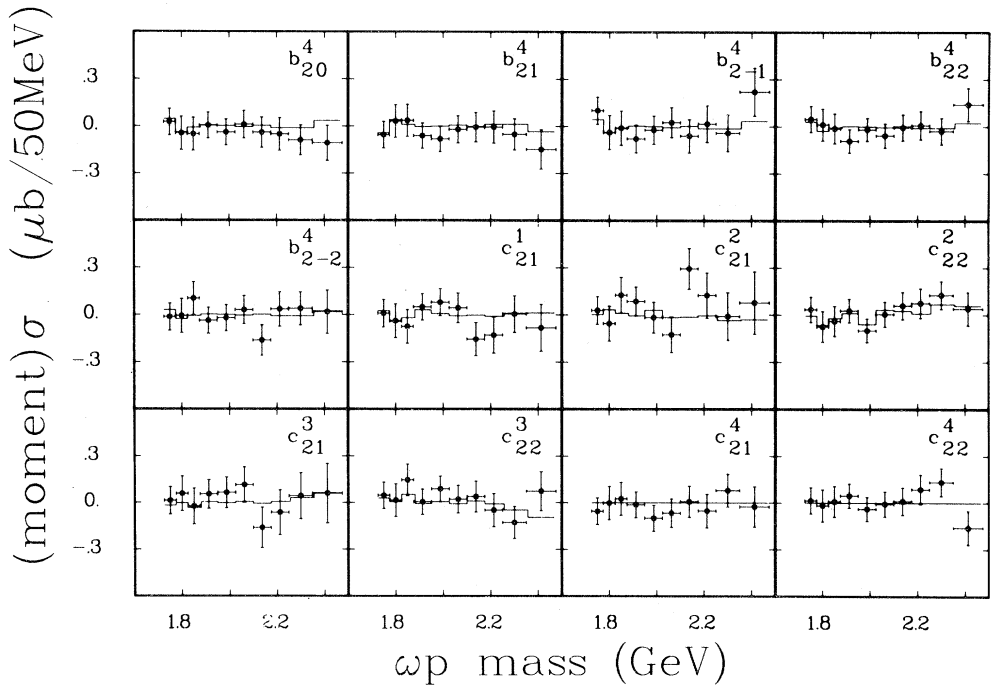

FIG. 7. (*Continued.*)

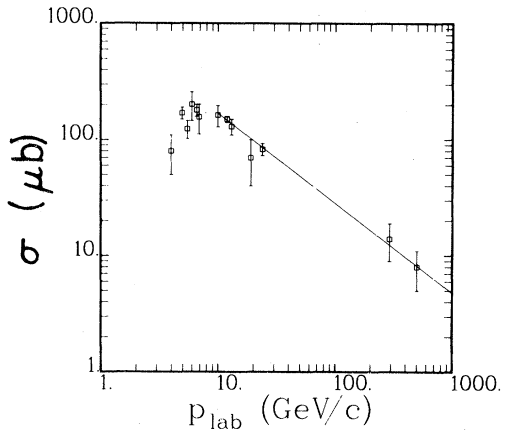

FIG. 8. The total cross section for the reaction $pp \rightarrow p\omega p$ versus beam momentum. The data points are from Refs. 11, 12, 22, and 27–34. The solid line is a fit of the form $p_{\text{lab}}{}^{-n}$ ($n = 0.77 \pm 0.07$) to the points with $p_{\text{lab}} \geq 10$ GeV/c.

used at 6 GeV/c was the same as at 11.75 GeV/c. The beam flux was such as to give a sensitivity of 1.51 events/nb for 100% acceptance. Only longitudinal beam polarization was used. The same procedures for extracting the ω signal were used as at 11.75 GeV/c. Figure 9 shows the $\pi^+\pi^-\pi^0$ mass distribution for the 6-GeV/c data. A fit to this distribution with a Gaussian plus a cubic-polynomial background yields 1063 ± 159 ω's with a Gaussian σ of 0.029 GeV.

The acceptance was calculated by Monte Carlo as at 11.75 GeV/c. The acceptance is slowly varying as a function of t over the t range of the data. However, the acceptance is flat in ωp mass only up to 1.8 GeV, above which it drops off rapidly. Thus it is impossible to examine the ωp mass distribution. The overall acceptance is about 2%.

Figure 10 shows the differential cross section $d\sigma/dt$ for ωp mass less than 1.9 GeV. Due to the low statistics, the moment calculation procedure was not used for these data; instead the acceptance was calculated for each t bin assuming isotropic angular distributions. The $d\sigma/dt$ shown in Fig. 10 is seen to have a similar shape to that at 11.75 GeV/c. There is again the suggestion of a dip around 0.2 GeV^2.

Thus the enhancement is seen to be produced with a t distribution and energy dependence consistent with ω exchange. We may therefore regard the ωp enhancement as being formed in virtual ωp elastic scattering.

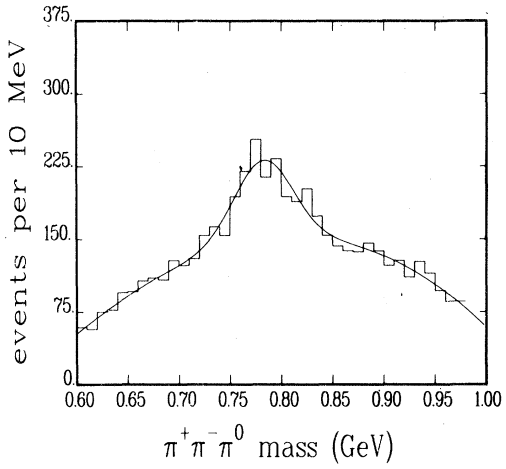

FIG. 9. The distribution of the $\pi^+\pi^-\pi^0$ mass in the reaction $pp \rightarrow p\pi^+\pi^-\pi^0 p$ at 6 GeV/c in the $-t$ range 0.075 to 0.5 GeV^2. Both solutions of the quadratic ambiguity are plotted if the ambiguity could not be resolved by the techniques described in the text. The curve is a fit to a Gaussian plus a cubic-polynomial background.

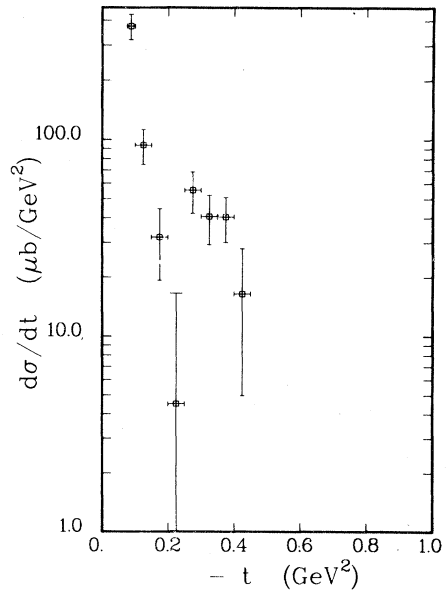

FIG. 10. The differential cross section for the reaction $pp \rightarrow p\omega p$, with subsequent ω decay to $\pi^+\pi^-\pi^0$ at 6 GeV/c and with ωp mass between 1.725 and 1.9 GeV. Acceptance corrections assumed isotropic decay distributions for the ωp and ω decays.

B. Spin and parity of the enhancement

An amplitude analysis was performed on the moments shown in Fig. 7 to determine the spin and parity content of the enhancement. The moments are proportional to sums of bilinear products of the production amplitudes. The unpolarized moments a_{ln}^L and the polarized moments b_{ln}^L and c_{ln}^L may be written as

$$a_{ln}^L = \sum K_{ij} \operatorname{Re}(A_i^* A_j) ,$$
$$b_{ln}^L, c_{ln}^L = \sum K_{ij} \operatorname{Im}(A_i^* A_j) , \tag{3}$$

where the A_i's are the production amplitudes and

TABLE I. Formulas relating the moments a_{ln}^L, b_{ln}^L, c_{ln}^L to the S- and P-wave amplitudes. The notation used for a product of amplitudes A_iA_j (e.g., $^1S_1\ ^1P_3$) is an abbreviation for $\operatorname{Re}(A_i^*A_j)$ for the a_{ln}^L moments and $\operatorname{Im}(A_i^*A_j)$ for the b_{ln}^L and c_{ln}^L moments. The coefficients of the terms were calculated numerically and are estimated to be accurate only to ±5%. The sign of the b_{ln}^L terms corresponds to pure natural-parity exchange; unnatural-parity exchange would give opposite signs for all b_{ln}^L terms.

$a_{00}^0 = +1.000\,{}^1S_1\,{}^1S_1 + 1.000\,{}^3S_3\,{}^3S_3 + 1.000{}^1P_1\,{}^1P_1 + 1.000\,{}^1P_3\,{}^1P_3 + 1.000\,{}^3P_1\,{}^3P_1$
$+ 1.000\,{}^3P_3\,{}^3P_3 + 1.000\,{}^3P_5\,{}^3P_5$
$a_{20}^0 = -1.202\,{}^3P_1\,{}^1P_1 + 0.414\,{}^3P_1\,{}^3P_1 + 0.380{}^3P_3\,{}^1P_3 - 0.351{}^3P_3\,{}^3P_3 + 0.074{}^3P_5\,{}^3P_5$
$a_{00}^1 = -1.115{}^1P_1\,{}^1S_1 - 1.633{}^1P_3\,{}^1S_1 + 1.000{}^3P_1\,{}^3S_3 - 0.518{}^3P_3\,{}^3S_3 - 1.548{}^3P_5\,{}^3S_3$
$a_{20}^1 = -0.694{}^1P_1\,{}^3S_3 - 0.098{}^1P_3\,{}^3S_3 + 0.694{}^3P_1\,{}^1S_1 + 0.478{}^3P_1\,{}^3S_3 - 0.310{}^3P_3\,{}^1S_1 + 0.181{}^3P_3\,{}^3S_3 - 0.114{}^3P_5\,{}^3S_3$
$a_{21}^1 = +0.916{}^1P_1\,{}^3S_3 + 0.130{}^1P_3\,{}^3S_3 - 0.916{}^3P_1\,{}^1S_1 - 0.648{}^3P_1\,{}^3S_3 + 0.410{}^3P_3\,{}^1S_1 - 0.232{}^3P_3\,{}^3S_3 + 0.174{}^3P_5\,{}^3S_3$
$a_{00}^2 = +1.000{}^1P_3\,{}^1P_1 + 0.447{}^1P_3\,{}^1P_3 - 0.398\,{}^3P_3\,{}^3P_1 - 0.360{}^3P_3\,{}^3P_3 - 1.194{}^3P_5\,{}^3P_1 + 0.539{}^3P_5\,{}^3P_3 + 0.356{}^3P_5\,{}^3P_5$
$a_{20}^2 = +0.538{}^3S_3\,{}^1S_1 + 0.190{}^3S_3\,{}^3S_3 - 0.760{}^3P_1\,{}^1P_3 + 0.240{}^3P_1\,{}^1P_1 + 0.170\,{}^3P_3\,{}^1P_3 - 0.166{}^3P_3\,{}^3P_1$
$+ 0.194\,{}^3P_3\,{}^3P_3 + 0.721{}^3P_5\,{}^1P_1 + 0.146{}^3P_5\,{}^1P_3 - 0.497{}^3P_5\,{}^3P_1 - 0.169{}^3P_5\,{}^3P_3 + 0.105{}^3P_5\,{}^3P_5$
$a_{21}^2 = -0.820{}^3S_3\,{}^1S_1 - 0.290{}^3S_3\,{}^3S_3 + 0.869\,{}^3P_1\,{}^1P_3 - 0.389{}^3P_3\,{}^1P_3 + 0.389{}^3P_3\,{}^3P_1 - 0.174\,{}^3P_3\,{}^3P_3 - 0.916{}^3P_5\,{}^1P_1$
$- 0.241\,{}^3P_5\,{}^1P_3 + 0.518{}^3P_5\,{}^3P_1 + 0.240{}^3P_5\,{}^3P_3 - 0.199{}^3P_5\,{}^3P_5$
$a_{22}^2 = +0.800\,{}^3S_3\,{}^1S_1 + 0.283{}^3S_3\,{}^3S_3 - 1.073{}^3P_1\,{}^1P_1 + 0.759\,{}^3P_3\,{}^1P_3 - 0.759{}^3P_3\,{}^3P_1 - 0.170\,{}^3P_3\,{}^3P_3$
$+ 0.358{}^3P_5\,{}^1P_1 + 0.289\,{}^3P_5\,{}^1P_3 + 0.253{}^3P_5\,{}^3P_1 - 0.210{}^3P_5\,{}^3P_3 + 0.291\,{}^3P_5\,{}^3P_5$
$a_{20}^3 = -0.578{}^1P_3\,{}^3S_3 - 0.259{}^3P_3\,{}^3S_3 - 0.610{}^3P_5\,{}^1S_1 - 0.345{}^3P_5\,{}^3S_3$
$a_{21}^3 = +0.831{}^1P_3\,{}^3S_3 + 0.372{}^3P_3\,{}^3S_3 + 0.876\,{}^3P_5\,{}^1S_1 + 0.496{}^3P_5\,{}^3S_3$
$a_{22}^3 = -0.641\,{}^1P_3\,{}^3S_3 - 0.287\,{}^3P_3\,{}^3S_3 - 0.676{}^3P_5\,{}^1S_1 - 0.382{}^3P_5\,{}^3S_3$
$a_{20}^4 = +0.652{}^3P_5\,{}^1P_3 + 0.291{}^3P_5\,{}^3P_3 + 0.146{}^3P_5\,{}^3P_5$
$a_{21}^4 = -0.907{}^3P_5\,{}^1P_3 - 0.406\,{}^3P_5\,{}^3P_3 - 0.203{}^3P_5\,{}^3P_5$
$a_{22}^4 = -0.626{}^3P_5\,{}^1P_3 + 0.280{}^3P_5\,{}^3P_3 + 0.140{}^3P_5\,{}^3P_5$
$b_{00}^1 = -1.155\,{}^1P_1\,{}^1S_1 + 0.816{}^1P_3\,{}^1S_1 - 0.574\,{}^3P_1\,{}^3S_3 + 1.000{}^3P_3\,{}^3S_3 - 0.774{}^3P_5\,{}^3S_3$
$b_{20}^1 = +0.347{}^1P_1\,{}^3S_3 + 0.196{}^1P_3\,{}^3S_3 + 0.694{}^3P_1\,{}^1S_1 - 0.239{}^3P_1\,{}^3S_3 + 0.155\,{}^3P_3\,{}^1S_1 - 0.363{}^3P_3\,{}^3S_3 - 0.057{}^3P_5\,{}^3S_3$
$b_{21}^1 = -0.324{}^1P_1\,{}^3S_3 - 0.183\,{}^1P_3\,{}^3S_3 - 0.648{}^3P_1\,{}^1S_1 + 0.229{}^3P_1\,{}^3S_3 + 0.648\,{}^3P_1\,{}^1P_1 + 0.229{}^3P_1\,{}^1P_3$
$- 0.145\,{}^3P_3\,{}^1S_1 + 0.328{}^3P_3\,{}^3S_3 - 0.290{}^3P_3\,{}^1P_1 + 0.082\,{}^3P_3\,{}^1P_3$
$+ 0.307{}^3P_3\,{}^3P_1 + 0.061\,{}^3P_5\,{}^3S_3 - 0.061{}^3P_5\,{}^1P_3 + 0.137{}^3P_5\,{}^3P_3$
$b_{2-1}^1 = +0.324\,{}^1P_1\,{}^3S_3 + 0.183{}^1P_3\,{}^3S_3 + 0.648{}^3P_1\,{}^1S_1 - 0.229\,{}^3P_1\,{}^3S_3 + 0.648{}^3P_1\,{}^1P_1 + 0.229\,{}^3P_1\,{}^1P_3$
$+ 0.145{}^3P_3\,{}^1S_1 - 0.328{}^3P_3\,{}^3S_3 - 0.290{}^3P_3\,{}^1P_1 + 0.082{}^3P_3\,{}^1P_3$
$+ 0.307{}^3P_3\,{}^3P_1 - 0.061{}^3P_5\,{}^3S_3 - 0.061{}^3P_5\,{}^1P_3 + 0.137\,{}^3P_5\,{}^3P_3$
$b_{00}^2 = -1.095\,{}^1P_3\,{}^1P_1 + 0.345{}^3P_3\,{}^3P_1 - 0.689\,{}^3P_5\,{}^3P_1 + 0.777{}^3P_5\,{}^3P_3$
$b_{20}^2 = +0.466{}^3S_3\,{}^1S_1 - 0.658{}^3P_1\,{}^1P_3 - 0.208{}^3P_3\,{}^1P_1 + 0.143{}^3P_3\,{}^3P_1 + 0.416{}^3P_5\,{}^1P_1$
$+ 0.210{}^3P_5\,{}^1P_3 - 0.287{}^3P_5\,{}^3P_1 - 0.244\,{}^3P_5\,{}^3P_3$
$b_{21}^2 = -0.502{}^3S_3\,{}^1S_1 - 0.251{}^1P_1\,{}^3S_3 - 0.177{}^3P_1\,{}^3S_3 + 0.532{}^3P_1\,{}^1P_3 + 0.337{}^3P_3\,{}^1S_1 - 0.238{}^3P_3\,{}^3P_1 + 0.075\,{}^3P_5\,{}^1S_1$
$- 0.075{}^3P_5\,{}^1S_1 + 0.132{}^3P_5\,{}^3S_3 + 0.374{}^3P_5\,{}^1P_1 + 0.246{}^3P_5\,{}^1P_3 - 0.212{}^3P_5\,{}^3P_1 - 0.245{}^3P_5\,{}^3P_3$
$b_{22}^2 = +0.490{}^3S_3\,{}^1S_1 + 0.490\,{}^1P_1\,{}^3S_3 + 0.346{}^3P_1\,{}^3S_3 - 0.657{}^3P_3\,{}^1S_1 + 0.657{}^3P_3\,{}^1P_1 + 0.465{}^3P_3\,{}^3P_1$
$- 0.146{}^3P_5\,{}^1S_1 + 0.258{}^3P_5\,{}^3S_3 + 0.146\,{}^3P_5\,{}^1P_1 + 0.295{}^3P_5\,{}^1P_3 + 0.103\,{}^3P_5\,{}^3P_1 - 0.214{}^3P_5\,{}^3P_3$
$b_{2-2}^2 = +0.490{}^3S_3\,{}^1S_1 - 0.490{}^1P_1\,{}^3S_3 - 0.346{}^3P_1\,{}^3S_3 + 0.657{}^3P_3\,{}^1S_1 + 0.657{}^3P_3\,{}^1P_1 + 0.465{}^3P_3\,{}^3P_1$
$+ 0.146\,{}^3P_5\,{}^1S_1 - 0.258{}^3P_5\,{}^3S_3 + 0.146{}^3P_5\,{}^1P_1 + 0.295\,{}^3P_5\,{}^1P_3 + 0.103{}^3P_5\,{}^3P_1 - 0.214{}^3P_5\,{}^3P_3$

TABLE I. (*Continued.*)

$b^3_{20} = +0.472\,{}^1P_3\,{}^3S_3 + 0.211\,{}^3P_3\,{}^3S_3 - 0.498\,{}^3P_5\,{}^1S_1 - 0.070\,{}^3P_5\,{}^3S_3$

$b^3_{21} = -0.480\,{}^1P_3\,{}^3S_3 - 0.215\,{}^3P_3\,{}^3S_3 - 0.322\,{}^3P_3\,{}^1P_3 + 0.506\,{}^3P_5\,{}^1S_1 + 0.072\,{}^3P_5\,{}^3S_3$
$- 0.253\,{}^3P_5\,{}^1P_1 - 0.179\,{}^3P_5\,{}^3P_1 - 0.040\,{}^3P_5\,{}^3P_3$

$b^3_{2-1} = +0.480\,{}^1P_3\,{}^3S_3 + 0.215\,{}^3P_3\,{}^3S_3 - 0.322\,{}^3P_3\,{}^1P_3 - 0.506\,{}^3P_5\,{}^1S_1 - 0.072\,{}^3P_5\,{}^3S_3$
$- 0.253\,{}^3P_5\,{}^1P_1 - 0.179\,{}^3P_5\,{}^3P_1 - 0.040\,{}^3P_5\,{}^3P_3$

$b^3_{22} = +0.370\,{}^1P_3\,{}^3S_3 + 0.166\,{}^3P_3\,{}^3S_3 + 0.497\,{}^3P_3\,{}^1P_3 - 0.390\,{}^3P_5\,{}^1S_1 - 0.055\,{}^3P_5\,{}^3S_3 + 0.390\,{}^3P_5\,{}^1P_1 - 0.028\,{}^3P_5\,{}^1P_3$
$+ 0.276\,{}^3P_5\,{}^3P_1 + 0.062\,{}^3P_5\,{}^3P_3$

$b^3_{2-2} = +0.370\,{}^1P_3\,{}^3S_3 + 0.166\,{}^3P_3\,{}^3S_3 - 0.497\,{}^3P_3\,{}^1P_3 - 0.390\,{}^3P_5\,{}^1S_1 - 0.055\,{}^3P_5\,{}^3S_3 - 0.390\,{}^3P_5\,{}^1P_1$
$+ 0.028\,{}^3P_5\,{}^1P_3 - 0.276\,{}^3P_5\,{}^3P_1 - 0.062\,{}^3P_5\,{}^3P_3$

$b^4_{20} = +0.515\,{}^3P_5\,{}^1P_3 + 0.230\,{}^3P_5\,{}^3P_3$

$b^4_{21} = -0.507\,{}^3P_5\,{}^1P_3 - 0.227\,{}^3P_5\,{}^3P_3$

$b^4_{2-1} = +0.507\,{}^3P_5\,{}^1P_3 + 0.227\,{}^3P_5\,{}^3P_3$

$b^4_{22} = +0.350\,{}^3P_5\,{}^1P_3 + 0.156\,{}^3P_5\,{}^3P_3$

$b^4_{2-2} = +0.350\,{}^3P_5\,{}^1P_3 + 0.156\,{}^3P_5\,{}^3P_3$

$c^1_{21} = -0.916\,{}^3P_1\,{}^1P_1 + 0.648\,{}^3P_1\,{}^1P_3 - 0.820\,{}^3P_3\,{}^1P_1 + 0.058\,{}^3P_3\,{}^1P_3$
$+ 0.869\,{}^3P_3\,{}^3P_1 + 0.174\,{}^3P_5\,{}^1P_3 - 0.389\,{}^3P_5\,{}^3P_3$

$c^2_{21} = +0.410\,{}^1P_1\,{}^3S_3 - 0.290\,{}^1P_3\,{}^3S_3 + 0.290\,{}^3P_1\,{}^3S_3 + 0.550\,{}^3P_3\,{}^1S_1$
$+ 0.259\,{}^3P_3\,{}^3S_3 - 0.183\,{}^3P_5\,{}^1S_1 + 0.130\,{}^3P_5\,{}^3S_3$

$c^2_{22} = -0.800\,{}^1P_1\,{}^3S_3 + 0.566\,{}^1P_3\,{}^3S_3 - 0.566\,{}^3P_1\,{}^3S_3 - 1.073\,{}^3P_3\,{}^1S_1$
$- 0.506\,{}^3P_3\,{}^3S_3 + 0.358\,{}^3P_5\,{}^1S_1 - 0.253\,{}^3P_5\,{}^3S_3$

$c^3_{21} = -0.558\,{}^3P_3\,{}^1P_3 + 0.438\,{}^3P_5\,{}^1P_1 - 0.124\,{}^3P_5\,{}^1P_3 + 0.310\,{}^3P_5\,{}^3P_1 + 0.277\,{}^3P_5\,{}^3P_3$

$c^3_{22} = +0.861\,{}^3P_3\,{}^1P_3 - 0.676\,{}^3P_5\,{}^1P_1 + 0.191\,{}^3P_5\,{}^1P_3 - 0.478\,{}^3P_5\,{}^3P_1 - 0.428\,{}^3P_5\,{}^3P_3$

the K_{ij}'s are constants; the detailed calculation of the K_{ij}'s is described in the Appendix, and numerical values are given in Table I. The amplitudes A_i in Eq. (3) are classified by the quantum numbers of the ωp system, namely the total spin S ($S = \frac{1}{2}$ or $\frac{3}{2}$), total angular momentum J, and total orbital momentum L; the ωp relative parity is $(-1)^{L+1}$. Adopting the spectroscopic notation $^{2S}L_{2J}$, there are two possible S waves, $^1S_1$ and $^3S_3$, and five P waves $^1P_1$, $^1P_3$, $^3P_1$, $^3P_3$, and $^3P_5$. We restrict our analysis to these waves, because the a^4_{00} moment, which is quadratic in the D waves, is consistent with zero. This assumption appears to be reasonable for low ωp masses, but should not be expected to give a complete description at higher masses, where the a^3_{00} moment indicates significant P-D interference.

A mass-independent amplitude analysis was performed on the moment data for the $|t|$ range 0.075 to 0.2 GeV^2. We have assumed t-channel helicity conservation and pure natural-parity exchange for the production amplitudes. We also assumed spin coherence at the recoil-proton vertex (as would be expected for ω or Pomeron exchange mechanisms). In each mass bin a 13-parameter fit was made to the 17 unpolarized, 22 transversely polarized, and 7 longitudinally polarized moments. The parameters were the real and imaginary parts of the seven S- and P-wave amplitudes. The overall phase was fixed by setting the $^1S_1$ amplitude to be purely real. The full correlated error matrix of the moments was used in calculating the χ^2.

The following procedure was used to obtain all possible solutions. In each ωp mass bin 1000 random values of the parameters (constrained so that the overall cross section was correct) were examined and the 20 sets having the best χ^2 were then used as starting values for the fitting program. All solutions found in this way were then checked for continuity with solutions in neighboring bins by using them (after suitable scaling) as starting points for fits in the neighboring bins. A rather large number of solutions was found, perhaps due to the large size of the errors. The χ^2's of the solutions were good; in no bin was the χ^2 worse than 1.5 per degree of freedom. Continuity was used to group the solutions into two overall continuous solutions throughout the entire mass range. We denote these as solutions A and B. The two

solutions are essentially identical in the mass bin 2.050 to 2.125 GeV, so there is some ambiguity in the continuation through this point.

The intensities and phases of the partial waves for solutions A and B are shown in Figs. 11 and 12; the agreement of solution A with the moments is shown in Fig. 7. The phases of the amplitudes in Figs. 11 and 12 are shown only for those bins where the intensity is substantially different from zero. We see that solution A is characterized by peaking at low mass in the $^3S_3$ and $^1P_3$ waves and smooth behavior in the other waves. The phases are relatively flat versus mass, and have values near 0 or π, i.e., the amplitudes are all relatively real. Solution B has low-mass peaking in the $^1S_1$ and $^3P_5$ waves and perhaps in the $^3S_3$ wave. Again the phases are all near 0 or π.

The main features of these two solutions in the low-mass region are required by the data as follows. The large value of a_{00}^2 results from the $^1P_3$ wave in solution A and from the $^3P_5$ wave in solution B. The peaking of the a_{20}^3, a_{21}^3, and a_{22}^3 moments results from interference of the $^3S_3$ and $^1P_3$ waves in solution A and of the $^1S_1$ and $^3P_5$ waves in solution B. The phases are restricted to being near 0 or π, i.e., the amplitudes being relatively real, by the fact that none of the polarization moments is substantially different from zero.

Of the two solutions, A shows somewhat smoother mass dependence than B. Solution B shows a large jump in the $^1P_3$ wave from zero at low mass to very large values above 2.2 GeV. Also solution B appears to require contributions from three waves $^3S_3$, $^1S_1$ and $^3P_5$ to account for the low-mass enhancement instead of the two waves $^3S_3$ and $^1P_3$ required by solution A. We know of no clearcut way to select the correct solution, but A is preferred on grounds of simplicity, and from here on we restrict our discussion to A.

The facts that the amplitudes of the $^3S_3$ and $^1P_3$ waves peak right at threshold and show no phase motion as the ωp mass increases suggest that the enhancement may be due to resonances with masses below the ωp threshold. The best candidate for the state producing the $^3S_3$ enhancement is the $N(1700)$ (D'_{13} in πp scattering analysis) with mass in the range 1.67 to 1.73 GeV and with width Γ in the range 0.07 to 0.12 GeV.[36] For the $^1P_3$ wave there is the $N(1810)$ (P'_{13} in πp). The most recent phase-shift analyses[37] give a mass of 1.7 GeV and a width of 0.125 GeV for this state. Previous studies of the production of such states have generally only provided cross sections for a bump near

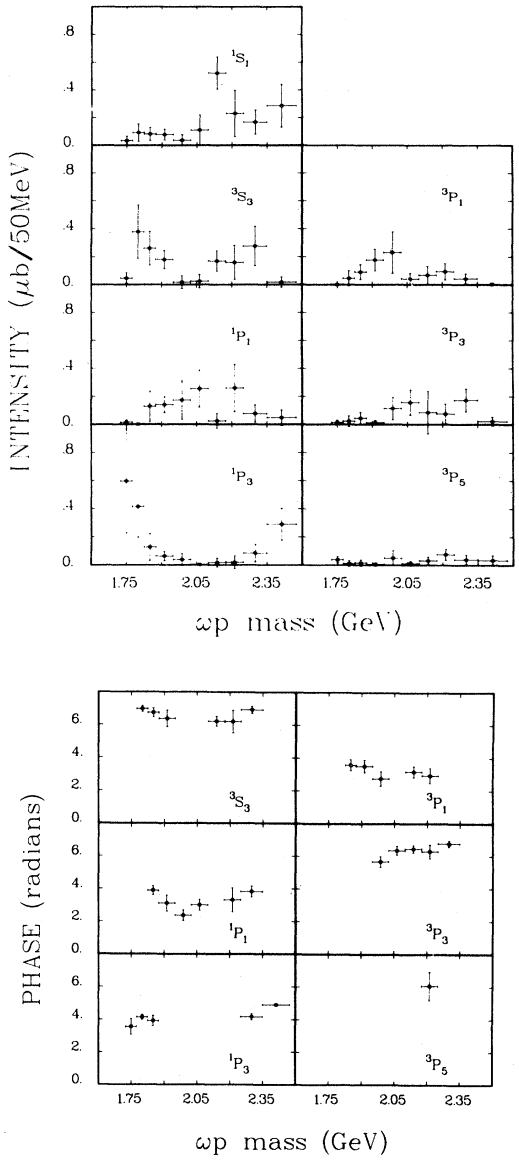

FIG. 11. The intensity and phase of the two *S*-wave and five *P*-wave amplitudes versus ωp mass for solution A of the amplitude analysis. The phase of the $^1S_1$ amplitude was fixed to be identically zero. Phases are plotted only for bins where the intensity of the amplitude is greater than 0.05 μb/50 MeV.

1.7 GeV without resolving it into its component spin-parity states.[38–40] Thus there is no basis for deriving branching ratios to ωp for these states. (Amplitude analysis of the $p\pi^+\pi^-$ final state using data obtained in the present experiment will in the future provide information on relative branching

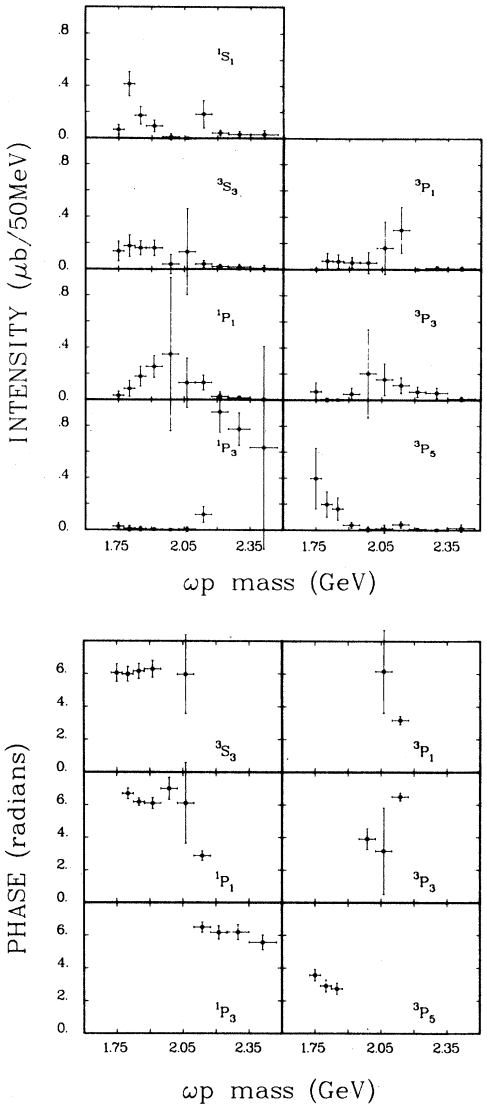

FIG. 12. Same as Fig. 11, but for solution B of the amplitude analysis.

ratios. In addition, the t dependence of the production of these states can be examined, which will confirm or deny the indications seen in the present experiment for an ω-exchange mechanism.)

We wish to emphasize that no evidence is seen for a narrow resonance near 1.8 GeV. The conclusion that the relative phases of the various waves are all near 0 or π, which is derived from the observation that all the polarization moments are consistent with zero, is an important part of this. To further illustrate this point we have calculated the polarization effects which would be expected for a narrow resonance interfering with a smooth background. Figure 13 shows selected moments for a resonance at 1.8 GeV with a width of 0.15 GeV in the $^1P_3$ wave interfering with either a flat background composed of equal amounts of $^1S_1$, $^3S_3$, and $^1P_1$ waves (solid line) or a background entirely in the $^3S_3$ wave (dashed line). The relative amounts of resonance and background were chosen to roughly fit the observed cross section a_{00}^0. Substantial polarization effects are predicted.

V. SUMMARY AND CONCLUSIONS

A sample of 20 000 events of the reaction $pp \to p\omega p$ at 11.75 GeV/c beam momentum has been obtained along with a smaller sample of 1000 events at 6 GeV/c. The total cross section for this reaction is measured to be 160 ± 35 μb at 11.75 GeV/c, in good agreement with earlier measurements. The distribution of events in ωp mass shows a narrow enhancement near threshold. The t distribution of all events has a break in slope about a dip position at $t \approx -0.2$ GeV^2. This structure is observed in the 6-GeV/c data as well as in the 11.75-GeV/c data. The production cross section for $pp \to p\omega p$ varies with laboratory momentum as $p_{\text{lab}}{}^{-0.8}$. These results suggest that the production mechanism of this reaction is primarily ω exchange.

The joint-decay-angular-distribution moments of the data as well as the correlations with transverse and longitudinal beam polarization have been extracted. The most prominent features of these moments in the region of the low-mass enhancement are relatively large values of the a_{00}^2 moment and the a_{20}^3, a_{21}^3, and a_{22}^3 moments. All of the polarization correlations are consistent with zero. An amplitude analysis of the moments in terms of the two S waves and five P waves of the ωp system has been performed. Two discrete solutions are found. The preferred solution has large values of the $^3S_3$ and $^1P_3$ waves near threshold. The mass dependence of the magnitudes of these amplitudes and the fact that their relative phases are found to be constant and near 0 or π indicate that these waves are the high-mass tails of resonances below threshold, presumably the states D_{13}' and P_{13}' seen in π-nucleon phase-shift analysis.

ACKNOWLEDGMENTS

We wish to acknowledge the technical assistance provided by I. Ambats, J. Dawson, L. Filips, and

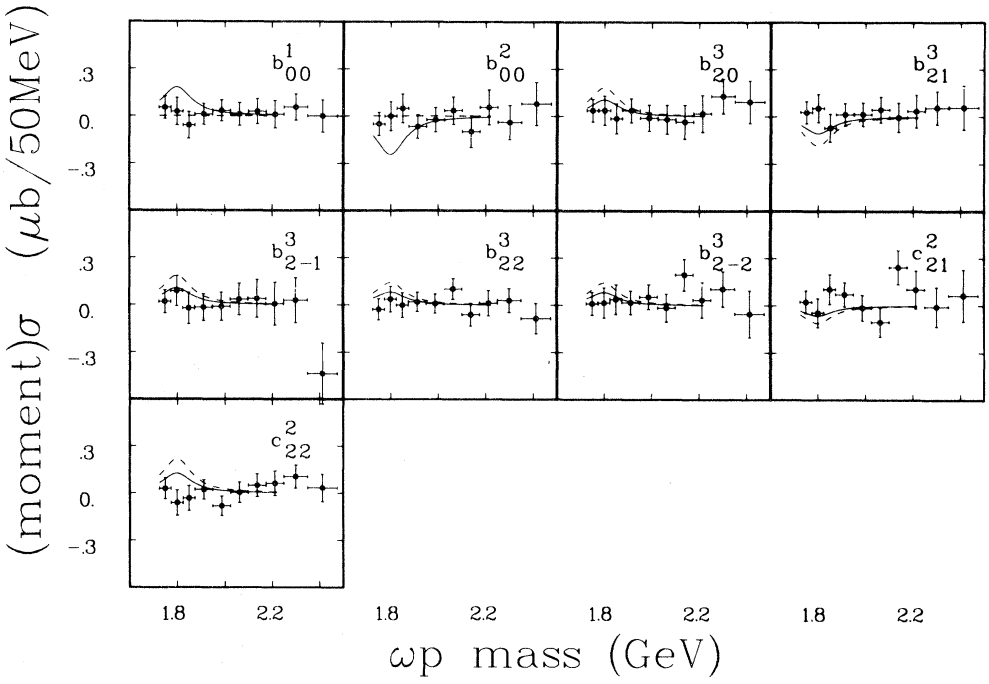

FIG. 13. Polarization effects in selected moments for a resonance in the $^1P_3$ wave with mass 1.8 GeV and width $\Gamma=0.15$ GeV interfering with a flat background, composed of either equal amounts of $^1S_1$, $^3S_3$, and $^1P_1$ waves (solid line), or only $^3S_3$ (dashed line). The data points are the same as in Fig. 7.

E. Walschon. We wish to thank R. Ely, C. Klindworth, R. Rivetna, and S. Watson for help with the online computers and the offline data processing. We thank the ZGS staff for the excellent operation of the accelerator and the Superconducting Magnet group for the construction of the spin-rotating solenoids. We would also like to thank N. Lockyer for help in the data taking. This work was supported by the U. S. Department of Energy.

APPENDIX

In this appendix we outline the derivation of the expansion given by Eq. (2), and the correspondence between observables and amplitudes in Table I. First we specify the coordinate system. We use the subscripts ω, b, f, t, and r to refer to the ω and to the beam, fast forward, target, and recoil protons, respectively. We denote by $\vec{p}_N$ the sum of the ω and forward-proton momenta. Three coordinate frames are needed and are defined as follows.

(1) In the ωp rest frame, the t-channel axes are

$$\hat{z}=\hat{p}_b,\ \hat{y}=\hat{p}_b\times\hat{p}_N,\ \hat{x}=\hat{y}\times\hat{z}\ , \tag{A1}$$

where all momentum vectors are evaluated in the ωp rest frame. The orientation of $\hat{p}_\omega$ in this frame is given by the angles $\Omega=\theta,\varphi$,

$$\begin{aligned}&\cos\theta=\hat{p}_\omega\cdot\hat{z},\ \sin\theta\cos\varphi=\hat{p}_\omega\cdot\hat{x}\ ,\\ &\sin\theta\sin\varphi=\hat{p}_\omega\cdot\hat{y}\ .\end{aligned} \tag{A2}$$

(2) In the ω rest frame (obtained by Lorentz transformation from the ωp rest frame), the axes are

$$\hat{z}'=-\hat{p}_f,\ \hat{y}'=\hat{z}\times\hat{z}',\ \hat{x}'=\hat{y}'\times\hat{z}'\ . \tag{A3}$$

The orientation of the ω-decay normal $\hat{n}_\omega$ in this frame is given by the angles $\Omega'=\theta',\varphi'$,

$$\begin{aligned}&\cos\theta'=\hat{n}_\omega\cdot\hat{z}',\ \sin\theta'\cos\varphi'=\hat{n}_\omega\cdot\hat{x}'\ ,\\ &\sin\theta'\sin\varphi'=\hat{n}_\omega\cdot\hat{y}'\ .\end{aligned} \tag{A4}$$

(3) In the beam-proton rest frame (obtained by

Lorentz transformation from the ωp rest frame), the t-channel axes are

$$\hat{z}''=\hat{p}_N,\ \hat{y}''=\hat{y},\ \hat{x}''=\hat{y}''\times\hat{z}'' . \tag{A5a}$$

($\hat{z}$ and $\hat{z}''$ are identical, since the transformation from the ωp_f rest frame to the p_b rest frame is along $\hat{z}$.) The beam polarization is most simply expressed in the s-channel frame, where

$$\hat{z}_s=-\hat{p}_t,\ \hat{y}_s=\hat{y},\ \hat{x}_s=\hat{y}_s\times\hat{z}_s . \tag{A5b}$$

The vector $\hat{p}_t$ in Eq. (A5) is p_t in the overall center-of-mass frame, boosted to the ωp_f and then to the p_b rest frames. Thus $\hat{z}_s$ and $\hat{z}''$ lie in a plane perpendicular to $\hat{y}$; we denote the crossing angle between $\hat{z}_s$ and $\hat{z}''$ by α. The beam polarization in the s channel has components

$$\begin{aligned} P_x^s&=P_\perp\sin\psi , \\ P_y^s&=P_\perp\cos\psi , \\ P_z^s&=P_{||} , \end{aligned} \tag{A6}$$

where $P_\perp$ and $P_{||}$ are transverse and longitudinal polarization components in the laboratory frame, and ψ is the orientation of the production normal $\hat{y}$ relative to the vertical axis in the laboratory. In the t channel the polarization components are

$$\begin{aligned} P_x^t&=P_\perp\cos\alpha\sin\psi-P_{||}\sin\alpha , \\ P_y^t&=P_\perp\cos\psi , \\ P_z^t&=P_\perp\sin\alpha\sin\psi+P_{||}\cos\alpha . \end{aligned} \tag{A7}$$

Thus, the transverse (P_x^t,P_y^t) and longitudinal (P_z^t) polarization components in the t channel are a mixture of $P_\perp$ and $P_{||}$. In principle our measured spin correlations, which are based on $\vec{P}^s$, could be unfolded to determine correlations with $\vec{P}^t$. In practice we have not done this because α is small, typically about 10° for the kinematic range of our experiment.

We next derive a general expression for observables in terms of production amplitudes A for the ωp partial waves. Each wave is characterized by the quantum numbers J (total spin), L (ωp orbital momentum), $(-1)^{L+1}$ (total ωp parity), and S (total ωp spin), collectively lumped into an index i. In addition, each ωp wave can be produced with different helicities (M), referred to the $\hat{x}$-$\hat{y}$-$\hat{z}$ frame; the helicities of the protons f, b, r, and t are designated, respectively, by indices ν, β, λ', and λ. The indices ν, λ', and λ are eventually summed over in forming observables. However, the beam proton is a coherent superposition of helicities $\beta=\pm 1/2$, depending on the polarization vector, and we denote these amplitude components by u_β. We ignore the ω-decay Dalitz plot dependence for simplicity. Then the transition amplitude describing production and breakup of the ωp system, followed by ω decay, can be expressed as

$$\langle\nu,\lambda'\,|\,T\,|\,u_\beta,\lambda\rangle=\sum_{M,\beta,i}A_{\lambda'\lambda}^{M\beta}(i)u_\beta F_M^\nu(i,\Omega,\Omega') . \tag{A8}$$

The functions F_M^ν describe the probability amplitude for the parent wave i to decay with angles Ω and Ω', and can be written as

$$F_M^\nu(i,\Omega,\Omega')=\frac{[(2L+1)(2j+1)]^{1/2}}{4\pi}\sum_\mu\langle S\mu,L0\,|\,J\mu\rangle\langle j\mu-\nu,\tfrac{1}{2}\nu\,|\,S\mu\rangle D_{\mu-\nu0}^{j*}(\varphi',\theta',0)D_{M\mu}^{J*}(\varphi,\theta,0) . \tag{A9}$$

Thus F_M^ν is a combination of probability amplitudes in which the fast-forward proton has spin component ν along $\hat{z}'$ and the ω has helicity μ-ν along $\hat{z}'$; the ω spin is exhibited explicitly as j ($j=1$). The arguments of the D functions, which differ from those used with the Jacob-Wick convention, are consistent with our choice of coordinate frames.[41]

We take the square of Eq. (A8) to derive the observed cross section as a function of the ωp mass m, momentum transfer t, and decay angles

$$\frac{d^6\sigma}{dt\,dm\,d\Omega\,d\Omega'}=\sum_{\nu,\lambda,\lambda',M,M',\beta,\beta',i,i'}[A_{\lambda'\lambda}^{M\beta}(i)A_{\lambda'\lambda}^{M'\beta'*}(i')][u_\beta u_{\beta'}^*][F_M^\nu(i,\Omega,\Omega')F_{M'}^{\nu*}(i',\Omega,\Omega')] . \tag{A10}$$

The first bracketed factor in Eq. (A10) contains the physics quantities which we wish to determine. The second factor is just the beam proton density matrix, namely

$$u_\beta u_{\beta'}^*=\tfrac{1}{2}[1+\vec{P}^t\cdot\sigma]_{\beta\beta'} , \tag{A11}$$

where P^t is given by Eq. (A7). The third factor contains all the angular dependence. It is convenient to define new helicity amplitudes that correspond asymptotically to natural ($\xi=+1$) and unnatural ($\xi=-1$) parity t-channel exchanges:

$$M^{M\beta}_{\lambda'\lambda}(i,\xi)=\frac{1}{\sqrt{2}}[A^{M\beta}_{\lambda'\lambda}(i) + \xi(-1)^{\Sigma S_j+M-\beta+L+1}A^{-M-\beta}_{\lambda'\lambda}(i)] , \tag{A12}$$

where $\Sigma S_j = J+\frac{3}{2}$ is the spin sum in the production process, and $(-1)^{L+1}$ is the relative intrinsic parity of the "particles" in the production process. Parity conservation relates the production amplitudes as follows:

$$A^{-M-\beta}_{-\lambda'-\lambda}(i)=(-1)^{\Sigma S_j+M+\beta-\lambda'-\lambda+L+1}A^{M\beta}_{\lambda'\lambda}(i) . \tag{A13}$$

Equation (A13) leads to the following relations for the naturality amplitudes:

$$M^{M\beta}_{\lambda'\lambda}(i)=\xi(-1)^{\lambda'-\lambda}M^{M\beta}_{-\lambda'-\lambda}(i) . \tag{A14}$$

Equation (A14) guarantees that there are no interference terms between $\xi=\pm1$ amplitudes in the cross section [Eq. (A10)], after summing over λ,λ'. Using Eq. (A12) and the properties of the Clebsch-Gordan coefficients and the rotation functions, we obtain the following symmetry relations:

$$M^{-M-\beta}_{\lambda'\lambda}(i,\xi)=\xi(-1)^{1/2+J+M-\beta+L}M^{M\beta}_{\lambda'\lambda}(i,\xi) , \tag{A15}$$

$$F^{-\nu}_{-M}(i,\Omega,\Omega')=(-1)^{1/2+J+M+\nu+L}F^{\nu*}_{M}(i,\Omega,\Omega') . \tag{A16}$$

These symmetries enable us to reduce the spin sum in Eq. (A10) to the expression

$$\frac{d^6\sigma(\xi)}{dt\,dm\,d\Omega\,d\Omega'}=\sum_{M,M',i,i'}\mathrm{Re}[M^{M(1/2)*}(i,\xi)M^{M'(1/2)*}(i',\xi)]\,\mathrm{Re}Z^{MM'}_{ii'}+\mathrm{Im}[M^{M(1/2)*}(i,\xi)M^{M'(1/2)*}(i',\xi)] \times[\xi(P^t_x\,\mathrm{Im}\tilde{Z}^{MM'}_{ii'}-P^t_y\,\mathrm{Re}\tilde{Z}^{MM'}_{ii'})+P^t_z\,\mathrm{Im}Z^{MM'}_{ii'}] , \tag{A17}$$

where $\sigma(\xi)$ splits off the contribution from each naturality. The functions $Z,\tilde{Z}$ contain all the angular dependence and are given by

$$Z^{MM'}_{ii'}=\sum_{\nu=\pm1/2}F^{\nu*}_{M}(i,\Omega,\Omega')F^{\nu*}_{M'}(i',\Omega,\Omega') , \tag{A18a}$$

$$\tilde{Z}^{MM'}_{ii'}=\sum_{\nu=\pm1/2}(-1)^{\nu-1/2}F^{\nu}_{M}(i,\Omega,\Omega')F^{-\nu}_{M'}(i',\Omega,\Omega') . \tag{A18b}$$

In Eq. (A17) we have shortened our notation, so that

$$M^{M(1/2)*}(i,\xi)M^{M'(1/2)}(i',\xi)=\sum_{\lambda'=\pm1/2}M^{M(1/2)*}_{\lambda'1/2}(i,\xi)M^{M'(1/2)}_{\lambda'1/2}(i',\xi) . \tag{A19}$$

Our normalization, implicit in Eqs. (A9) and (A12), is such that integration over Ω and Ω' yields

$$\frac{d^2\sigma(\xi)}{dm\,dt}=\sum_{M,i}M^{M(1/2)*}(i,\xi)M^{M(1/2)}(i,\xi) . \tag{A20}$$

So far, Eq. (A17) is completely general. We can achieve some further simplification by approximating the transverse polarization components with Eq. (A6) and substituting in Eq. (A17),

$$P^t_x\,\mathrm{Im}\tilde{Z}^{MM'}_{ii'}-P^t_y\,\mathrm{Re}\tilde{Z}^{MM'}_{ii'}\approx-P_\perp\,\mathrm{Re}[e^{i\psi}\tilde{Z}^{MM'}_{ii'}] . \tag{A21}$$

In our amplitude analysis we further assumed t-channel helicity conservation; this means that only $M=M'=\frac{1}{2}$ terms are needed in Eq. (A17). With this assumption, and using closure relations for products of D functions, we can deduce a general expansion for Z and $\tilde{Z}$ in terms of a set of orthogonal functions

$$\mathrm{Re}[Z^{(1/2)(1/2)}_{ii'}(\Omega,\Omega')]=\frac{1}{16\pi^2}\sum_{l,L,n}\alpha^{ii'}_{Lln}\{f_n[(2L+1)(2l+1)]^{1/2}\cos n\varphi' d^l_{n0}(\theta')d^L_{0n}(\theta)\} , \tag{A22a}$$

$$\mathrm{Im}[Z^{(1/2)(1/2)}_{ii'}(\Omega,\Omega')]=\frac{1}{16\pi^2}\sum_{l,L,n}\gamma^{ii'}_{Lln}\{f_n[(2L+1)(2l+1)]^{1/2}\sin n\varphi' d^l_{n0}(\theta')d^L_{0n}(\theta)\} , \tag{A22b}$$

$$\mathrm{Re}[e^{i\psi}\tilde{Z}^{(1/2)(1/2)}_{ii'}(\Omega,\Omega')]=\frac{1}{16\pi^2}\sum_{l,L,n}(-\beta^{ii'}_{Lln})\{[2(2L+1)(2l+1)]^{1/2}\cos(\psi+\varphi+n\varphi')d^{l}_{|n|0}(\theta')d^{L}_{1n}(\theta)\}\ , \tag{A22c}$$

where $f_n=1$ $(n=0)$, $\sqrt{2}$ $(n\neq 0)$. The functions in brackets are orthogonal and their square integrals over Ω and Ω' are equal to $16\pi^2$. The summation extends over $L=0$ to $L_{\max}$ and $l=0$ or 2; for expansions (A22a) and (A22b), only $n=0,1,2$ are required, while for (A22c), $n=-1,-2$ are needed in addition. Since $d^{l}_{n0}(\theta')$ and $d^{l}_{-n0}(\theta')$ are equal within a sign, we have used $d^{l}_{|n|0}(\theta')$ in Eq. (A22c).

We have computed the coefficients α, β, and γ numerically for each pair of waves i,i'; to do this, we compute the functions Z and $\tilde{Z}$ numerically using Eq. (A18), and project out each of the orthogonal functions in Eq. (A22) by numerical integration. For example,

$$\alpha^{ii'}_{Lln}=\int \mathrm{Re}Z^{(1/2)(1/2)}_{ii'}(\Omega,\Omega')\{f_n[(2L+1)(2l+1)]^{1/2}\cos n\varphi' d^{l}_{n0}(\theta')d^{L}_{0n}(\theta)\}d\Omega\, d\Omega' \tag{A23}$$

with similar relations for β and γ. By comparison with Eq. (A17), we see that the coefficients α, β, and γ are basically just the coefficients in Table I. [Note that the interference terms with $i\neq i'$ in Eq. (A17) occur twice, and the coefficients in Table I are then twice the corresponding α, β, or γ values.] Note also that the unnatural-parity contributions, which we have assumed to be negligible in our amplitude analysis, would contribute with opposite sign to the transverse polarization correlations [cf. Eq. (A17)]; this is equivalent to using the β's in Table I with opposite sign.

Finally, by substituting the expansions of Eq. (A22) into Eq. (A17) and summing over all waves, we obtain the general form for the observables given by Eq. (2) in the text. It is interesting to note that the only dependence of the observables on φ is through the correlation with $\psi+\varphi$ in the transverse polarization correlation [cf. Eq. (A22c)]. The angle $\psi+\varphi$ gives the azimuth between the transverse spin vector and the axis $\hat{y}'$, which is the normal to the virtual scattering process $p_b+e\rightarrow\omega+p_f$ (e denotes the t-channel exchange). Helicity conservation in the production of the ωp system ensures that there can be no alignment of the overall production normal with the beam spin [e.g., no terms of the form $\cos\psi$ in Eq. (A22c)]; in effect helicity conservation implies that e acts like a spin-0 particle in the virtual process. Nevertheless, there can be polarization effects in the virtual process due to interference of different N^*'s, which in effect cause helicity-flip transitions between p_b and p_f or p_b and ω. Similarly, we note that longitudinal spin correlations arise only in the $n\neq 0$ terms [cf. Eq. (A22b)], and if the ω were spinless, these terms would vanish. In effect, the longitudinal correlations are essentially spin-rotation parameters in the virtual process.

*Present address: Bell Laboratories, Naperville, Ill. 60540.

[1]F. J. Nagy, Ph.D. thesis, California Institute of Technology, 1980, Report No. CALT-68-757 (unpublished).
[2]M. S. Milgram *et al.*, Nucl. Phys. B18, 1 (1970).
[3]L. K. Sisterson *et al.*, Nucl. Phys. B48, 493 (1972).
[4]V. Davidson *et al.*, Phys. Rev. Lett. 32, 855 (1974).
[5]R. E. Juhala *et al.*, Phys. Rev. 184, 1461 (1969).
[6]C.-Y. Chien *et al.*, Nucl. Phys. B104, 189 (1976).
[7]P. J. Davis *et al.*, Nucl. Phys. B44, 344 (1972).
[8]P. Theocharopoulos *et al.*, Nucl. Phys. B83, 1 (1974).
[9]C. O. Wohl *et al.*, Nucl. Phys. B132, 401 (1978).
[10]H. W. Atherton *et al.*, Nuovo Cimento 30A, 505 (1975).
[11]E. Colton and E. Gellert, Phys. Rev. D 1, 1979 (1970).
[12]J. Le Guyader *et al.*, Nucl. Phys. B35, 573 (1971).
[13]R. Lednicky, Phys. Lett. 58B, 89 (1975).
[14]N. Isgur and G. Karl, Phys. Rev. D 19, 2653 (1979).
[15]R. Koniuk and N. Isgur, Phys. Rev. D 21, 1868 (1980).
[16]T. Khoe *et al.*, Part. Accel. 6, 213 (1975).
[17]D. Ayres, in *Proceedings of the International Conference on Instrumentation for High Energy Physics, Frascati, Italy, 1973,* edited by S. Stipcich (Laboratori Nazionali del Comitato Nazionale per l' Energia Nucleare, Frascati, Italy, 1973), p. 655.
[18]I. Ambats *et al.*, Nucl. Instrum. Meth. 174, 427 (1980).
[19]H. Hinterberger *et al.*, Rev. Sci. Instrum. 41, 413 (1970).
[20]B. C. Maglic *et al.*, Phys. Rev. 125, 687 (1962).

[21]A. B. Wicklund *et al.*, Phys. Rev. D 17, 1197 (1978).
[22]V. Blobel *et al.*, Nuc. Phys. B69, 237 (1974).
[23]J. Biel *et al.*, Phys. Rev. Lett. 36, 504 (1976); 36, 507 (1976); Phys. Lett. 65B, 291 (1976).
[24]H. de Kerret *et al.*, Phys. Lett. 63B, 477 (1976); 63B, 483 (1976).
[25]E. L. Berger and P. Pirila, Phys. Lett. 59B, 361 (1975).
[26]I. Ambats *et al.*, Phys. Rev. D 9, 1179 (1974).
[27]L. Bodini *et al.*, Nuovo Cimento 58A, 475 (1968).
[28]A. P. Colleraine and U. Nauenberg, Phys. Rev. 161, 1387 (1967).
[29]G. Alexander *et al.*, Phys. Rev. 154, 1284 (1967).
[30]C. Caso *et al.*, Nuovo Cimento 55A, 66 (1968).
[31]G. Yekutieli *et al.*, Nucl. Phys. B18, 301 (1970).
[32]S. P. Almeida *et al.*, Phys. Rev. 174, 1638 (1968).
[33]Zh. S. Takibaev *et al.*, Yad. Fiz. 20, 964 (1974). [Sov. J. Nucl. Phys. 20, 512 (1974)].
[34]J. C. M. Armitage *et al.*, Phys. Lett. 82B, 149 (1979).
[35]C. Daum *et al.*, Phys. Lett. 89B, 281 (1980).
[36]Particle Data Group, Rev. Mod. Phys. 52, S1 (1980).
[37]R. Cutkosky, in *Baryon 1980,* proceedings of the IVth International Conference on Baryon Resonances, Toronto, edited by N. Isgur (Univ. of Toronto Press, Toronto, 1981), p. 19.
[38]G. Cocconi *et al.*, Phys. Lett. 8, 134 (1964).
[39]U. Amaldi *et al.*, Phys. Lett. 34B, 435 (1971).
[40]R. M. Edelstein *et al.*, Phys. Rev. D 5, 1073 (1972).
[41]J. D. Jackson, in *High Energy Physics, 1965 Les Houches Lectures,* edited by C. DeWitt and M. Jacob (Gordon and Breach, New York, 1966), p. 325.